INSTITUT DE FRANCE
Académie des sciences

Comptes Rendus

Mécanique

Ju Liu, Junwei Yu, Lingbing Kong, Yonghui Guo, Hang Yu and Kuo Yuan

Study on the drag reduction mechanism of spheres with various hydrophobic types

Volume 350 (2022), p. 171-189

https://doi.org/10.5802/crmeca.110

CENTRE MERSENNE

Les Comptes Rendus. Mécanique *sont membres du*
Centre Mersenne pour l'édition scientifique ouverte
www.centre-mersenne.org
e-ISSN : 1873-7234

Comptes Rendus
Mécanique
2022, 350, p. 171-189
`https://doi.org/10.5802/crmeca.110`

Short paper / *Note*

Study on the drag reduction mechanism of spheres with various hydrophobic types

Ju Liu [a], **Junwei Yu** [*, a, b], **Lingbing Kong** [b], **Yonghui Guo** [a], **Hang Yu** [c]
and Kuo Yuan [a]

[a] College of Aerospace and Civil Engineering, Harbin Engineering University, Harbin 150001, China

[b] Beijing Institute of Aerospace Control Devices, Beijing 100094, China

[c] Yunnan Kunchuan Electronic Equipment Co., Ltd., Kunming Yunnan 650236, China

E-mails: liujuheu@163.com (J. Liu), yujunweiheu@163.com (J. Yu),
pengkezhenheu@163.com (L. Kong), guoyonghuiheu@126.com (Y. Guo),
838210999@163.com (H. Yu), yuankuoheu@163.com (K. Yuan)

Abstract. In this paper, a 3D hydrophobic model was developed using User-Defined Functions to investigate the flow characteristics and drag reduction mechanism of spheres with various hydrophobic types. The results confirmed that for the fully hydrophobic spheres, the separation point was continuously shifted back and the separation angle was reduced from 57.6° to 29.5° when the dimensionless slip length was increased from 0.02 to 0.1. The length of the recirculation zone was reduced from 1.90D to 0.93D, which was 51% shorter. And the decreasing fluctuation energy made the vortex structure transformed from hairpin-shaped vortices to vortex-ring. In addition, the drag reduction of partial-hydrophobic spheres was closely related to the number and location of the sudden change interfaces.

Keywords. Sphere, Hydrophobic, Drag reduction mechanism, Vortex structure, Separation point, Slip length.

Manuscript received 10th July 2021, revised 24th March 2022, accepted 11th April 2022.

1. Introduction

In engineering applications, especially in ocean engineering fields, drag reduction is a crucial topic, which is an effective method for the purpose of achieving various goals such as low energy consumption, long range voyage, and so on. Recently, drag reduction technology have made some significant progress, including drag-reducing additives [1,2], surface treatment [3–5], and air-injection [6, 7]. Among these methods, superhydrophobic surfaces have attracted great attention due to its potential for significant drag reduction, simple fabrication (spraying), low cost and strong antifouling ability [8–10].

Most of the inspirations of superhydrophobic surface come from plants, such as the superhydrophobic surface of lotus leaf, rice leaf or water strider leg [11, 12]. The superhydrophobic

---

[*] Corresponding author.

surface has micro or nanometer-sized surface features, and the chemical hydrophobicity of the material prevents the water from moving into the space between the peaks of the rough surface, resulting in the air–water interface which is essentially shear-free [13, 14]. The resulting surface possesses a composite interface where momentum transfer with the wall occurs only at liquid–solid and not the liquid–vapor interfaces [15]. Rothstein *et al.* [16, 17] measured the deflection of an air–water interface that is formed between microposts and supported by surface tension using a confocal surface metrology system, and presented the flow kinematics of water past drag-reducing superhydrophobic surfaces through microparticle image velocimetry. Martell [18] further confirmed by DNS simulation in turbulent channel flow that there is gas–liquid interface on superhydrophobic surface, for the largest microfeature spacing, an average slip velocity over 75% of the bulk velocity was obtained, and the wall shear stress reduction was found to be nearly 40%. Furthermore, Zhang [19] measured and studied turbulent flows over a superhydrophobic surface and a smooth surface. The results show that, in the near wall region, the turbulent coherent structures over the superhydrophobic surface are more stable and flat, due to the suppression in the strength and the lifting effect of the hairpin vortex. Rowin [20] presented a series of experiments to demonstrate drag reduction for the flow through microchannels using superhydrophobic surfaces with random surface microstructure, determined the drag reduction rate and slip length of each surface. Castagna [21] reported an experimental investigation of free falling super-hydrophobic (SH) spheres in glycerine–water mixtures over a wide range of Reynolds number, and emphasised the key role of the surface roughness properties on the triggering of wake instabilities.

Most researches on superhydrophobic surfaces focus on microchannel flow or rotating flow between plates. The exploration of the external flow around a superhydrophobic surface is relatively scarce, because the external flow around hydrophobic surface involves large geometry dimensions, wide flow fields, and undetermined wall shear stress, which makes it difficult to establish the geometric model and perform the numerical simulation. However, the proposed Navier slip model makes the numerical simulation of the external flow over a superhydrophobic surface be implemented [22]. The model considers that the magnitude of the slip velocity at the superhydrophobic surface is proportional to the local values of shear stress and slip length. Legendre [23] studied numerically the two-dimensional flow past a circular cylinder as a prototypical transitional flow, and investigated the influence of a generic slip boundary condition on the wake dynamics. Daniello [24] and Seo [25] investigated how the changes in vortex shedding and separation previously observed on superhydrophobic cylinders affects the rms lift force and the resulting oscillations induced on an elastically mounted cylinder. Huang [26] and Li [27] conducted the effect of dimensionless slip length and slip distribution on total, viscous and pressure drag coefficients of the cylinder. It is found that the viscous drag plays a major role in drag reduction, for low Reynolds ($\mathrm{Re} < 100$) and small slip length ($L_s < 0.02$). Zeinali [28] investigated the effect of imposing the locally partial-slip on the surface of the backward-facing step and the sphere. Dhiman [4] investigated a three-dimensional flow around two Janus spheres held fixed relative to each other with the line connecting their centres normal to a uniform fluid stream, at Reynolds numbers ranging from 0.1 to 50.

It can be seen that most of the existing numerical simulations are based on one-dimensional hydrophobic plate or two-dimensional hydrophobic cylinder, and the study of flow around a three-dimensional superhydrophobic structure is worthy of further exploration. Therefore, the flow characteristics of three-dimensional hydrophobic sphere at medium Reynolds number were explored in this paper. The effects of various slip lengths on the drag coefficient, Strouhal number, and wall shear stress of the sphere at $\mathrm{Re} = 400$ were analyzed in detail. The relationship between vortex structure and slip length was presented. In addition, the drag reduction effects and mechanisms of five types slip distribution were also studied.

This paper is organized as follows. The mathematical formulations, physical problems, and numerical methodology are described in Section 2. In Section 3, the accuracy of the numerical scheme and the slip model are verified. Subsequently, in Section 4.1, for the all slip sphere, the relationships between the drag reduction and slip length are explored, the pertinent parameters and vortex structures at various slip lengths are studied. In Section 4.2, the best partial-hydrophobic distribution scheme and the drag reduction mechanism of the different slip distributions are discussed. Section 5 summarizes the conclusions of this study.

2. Mathematical formulation and numerical methodology

2.1. *Numerical methods*

The continuity equation and momentum equation of incompressible viscous fluid are as follows:

$$\begin{gathered}\nabla\cdot\boldsymbol{V}=0\\ \frac{\partial\boldsymbol{V}}{\partial t}+(\boldsymbol{V}\cdot\nabla)\boldsymbol{V}=\boldsymbol{f}-\frac{1}{\rho}\nabla P+\frac{1}{\rho}\nabla\cdot(2\mu\boldsymbol{S})\end{gathered}\tag{1}$$

where μ is dynamic viscosity, ρ is the fluid density, $\boldsymbol{f}$ represents the volume force, $\boldsymbol{V}$ is the velocity vector, P presents pressure, $\boldsymbol{S}=((\nabla\boldsymbol{V})^T+\nabla\boldsymbol{V})/2$ denotes the rate-of-strain tensor.

In order to model the superhydrophobic condition over sphere, the impermeability and slip boundary conditions [23] has been implemented on the surface of the sphere through the User-Defined Functions, which read

$$\begin{gathered}\boldsymbol{n}\cdot\boldsymbol{V}=0\\ \boldsymbol{n}\times\boldsymbol{V}=2l_s\boldsymbol{n}\times(\boldsymbol{S}\cdot\boldsymbol{V})\end{gathered}\tag{2}$$

where $\boldsymbol{n}$ is the unit normal to the sphere surface, l_s is the sphere slip length. In this paper, the governing equation of the slip model has been applied to solve the flow characteristics of a hydrophobic sphere in spherical coordinate system, which is shown in Figure 1. After expanding (2) in the spherical coordinate system, the slip velocity in the directions of r, θ and φ can be obtained:

$$\begin{cases}u_r=0\\ u_\theta=l_s\dfrac{\partial u_\theta}{\partial r}\\ u_\varphi=l_s\dfrac{\partial u_\varphi}{\partial r}.\end{cases}\tag{3}$$

Finally, the slip velocities in the three directions in (3) are applied to the surface of hydrophobic spheres as boundary conditions to study the drag reduction mechanism of a hydrophobic spheres.

Two dimensionless parameters are involved in this study: Reynolds number, $\mathrm{Re}=\rho UD/\mu$, and the Strouhal number, $\mathrm{St}=fD/U$. Here U is the fluid velocity, D is the diameter of the sphere, and f is the frequency of vortex shedding. The drag coefficient C_d is defined as: $C_d=F_d/0.5\rho U^2A$, the lift coefficient C_l is: $C_l=F_l/0.5\rho U^2A$, and the pressure coefficient is: $C_p=P-P_\infty/0.5\rho U^2$. Here A is the cross-sectional area of the sphere, U is the fluid velocity in the far field, F_d is the time-averaged drag acting on the surface, F_l is the time-averaged lift, P is time-averaged pressure acting on the surface, and P_∞ is the ambient pressure.

2.2. *Numerical background and mesh set-up*

In the present study, we studied the effects of various slip lengths and slip distributions on the flow characteristics past a 3D sphere. The computational domain and geometric model have

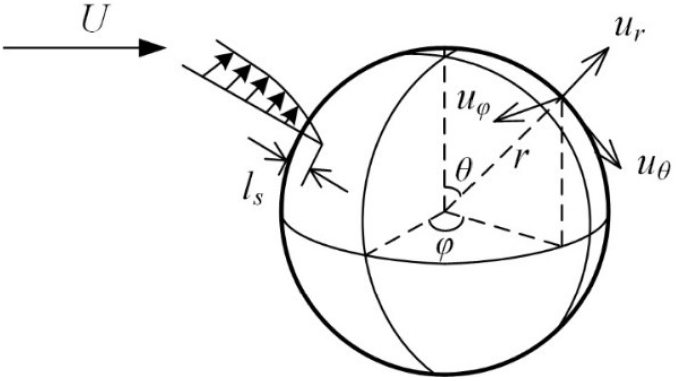

Figure 1. Sketch of velocity profile near sphere surface for slip length l_s. u_r, u_θ, u_φ are the components of the velocity vector in three directions, r, θ and φ, respectively.

Table 1. Details of the mesh topology and results of grid convergence study for flow over sphere at the Reynolds number of 400

Mesh	N_{total}	N_{sur}	δ	C_d	St
Mesh1	995,673	$50*30*30$	0.003D	0.701	0.132
Mesh2	2,549,208	$80*60*60$	0.002D	0.600	0.139
Mesh3	3,675,298	$100*80*80$	0.001D	0.600	0.140

been established as shown in Figure 2(a). The sphere is fixed in a tunnel with a length, breadth, and height of 80D, 20D, and 20D, respectively. The diameter of sphere is D. The velocity inlet is located at 20D upstream of the center of the sphere, and the velocity value is set according to Reynolds number range of 400 to 2000. The pressure outlet is located at 60D downstream of the center of the sphere. The wall of sphere is set as superhydrophobic surface, and the level of hydrophobicity is determined according to the slip length. The slip length can be regarded as a constant, which does not change with the wall shear stress [29]. Vast range of slip lengths has been reported in experimental and numerical researches, such as: Song *et al.* [13] reported 0.02 mm and Jian *et al.* [30] reported 0.04 mm slip length in their measurements. Larger slip lengths also have been reported in academic researches, i.e. 0.1 mm by Lee and Kim [31], 0.05–0.25 mm by Murai [32]. Therefore, the slip length range from 0.02 mm to 0.2 mm has been adopted in this paper.

A reasonable number of grids is needed to tradeoff the accuracy and cost of numerical calculation. In this paper, the mesh-independence studies have been accomplished at the Reynolds number of 400, and the results are available in Table 1. Where N_{total} is the total number of nodes, N_{sur} is the number of nodes on the sphere surface and δ is the thickness of cells closest to the cylinder surface. The drag coefficients and Strouhal numbers have been monitored at coarse mesh (Mesh1), fine mesh (Mesh2), and finest mesh (Mesh3). The results show that the differences between meshes Mesh2 and Mesh3 are negligible. Hence, Mesh2 is used as the final mesh. The boundary layer mesh near sphere has been presented in Figure 2(b), all meshes with a $y+$ value of less than 1, and a three-dimensional mesh distribution of the computational domain as shown in Figure 2(c).

The commercial Computational Fluid Dynamics codes ANSYS FLUENT 19.0 has been employed to conduct the simulations in the present work, with the slip model input through

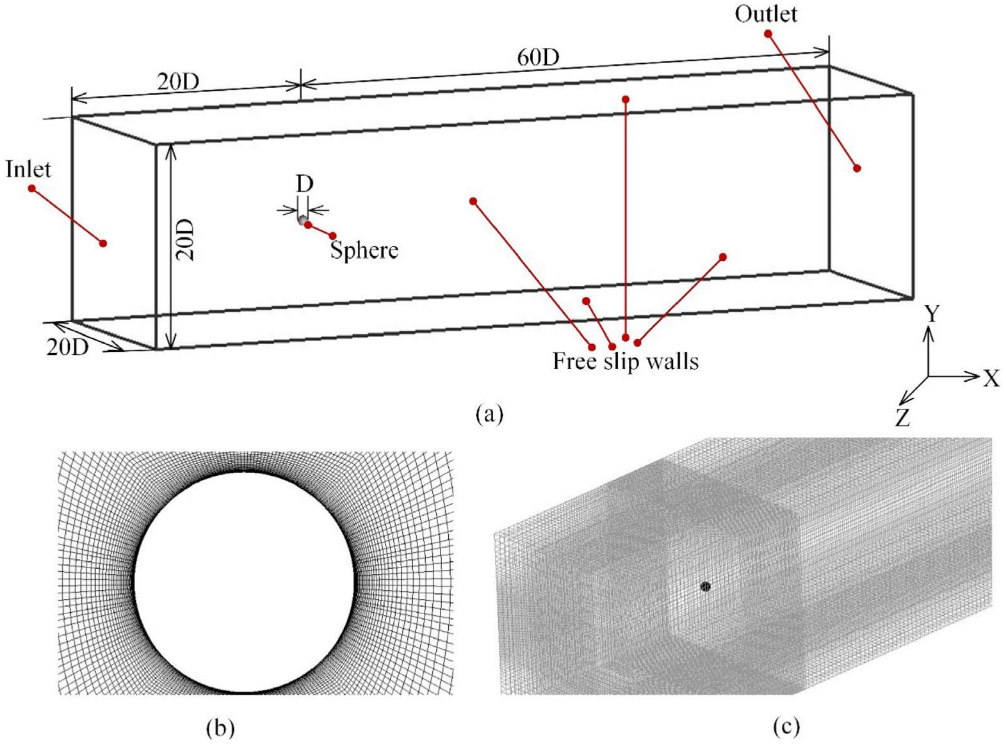

Figure 2. (a) Geometrical details and boundary conditions of the computational domain for flow over sphere, (b) a close snapshot of the boundary layer mesh near sphere, (c) a three-dimensional perspective view of the mesh.

User-Defined Functions. These commercial codes has been proven by a large number of scholars to perform with high accuracy on similar fluid mechanical problems. Including Taylor vortex flow [33], flow past a static or rotating circular cylinder [34, 35], and cavitating flow around a 3D hydrofoil [36]. For the present study, the range of Reynolds number is from 400 to 2000, and the flow in this range is laminar, so the laminar model is used to solve the flow governing equations. The PISO algorithm (Pressure Implicit with Splitting of Operators) has been adopted to solve the pressure-velocity coupling. The tolerance of convergence is 1×10^{-7}, and thirty iterations per time step have been used to achieve a tradeoff between the accuracy and efficiency. All calculations have been performed in a manner that average Courant number in the computational domain does not surpass 1.

3. Validation for CFD simulation

3.1. *Validation of numerical method*

The numerical schemes have been verified by comparing the Strouhal number and the drag coefficient calculated from the present simulation of flow over the no-slip sphere with the existing experimental results [37–39] at the Reynolds number of 400, and the results are listed in Table 2. The current predictions are in good agreement with the experimental results, and the average relative error of the drag coefficient and Strouhal number are less than 5% and 3%, respectively.

Table 2. Comparison of Strouhal number and drag coefficient for the no-slip sphere with the existing experimental data at the Reynolds number of 400

	C_d	St
Tomboulides *et al.* [38]	0.62	—
Margarvey and Bishop [39]	—	0.143
Wu [37]	0.603	—
The present study	0.600	0.139

Table 3. Comparison of drag coefficient and RMS of lift coefficient with the available data, the dimensionless slip lengths of the cylinder wall are 0.02 and 0.05, and the Reynolds numbers are 100 and 180, respectively

		C_d		$C_{l,\text{rms}}$	
		$L_s = 0.02$	$L_s = 0.05$	$L_s = 0.02$	$L_s = 0.05$
Re = 100	Huang *et al.*	1.262	1.112	0.203	0.139
	The present study	1.271	1.091	0.210	0.138
Re = 180	Huang *et al.*	1.216	0.993	0.378	0.249
	The present study	1.219	0.967	0.376	0.249

3.2. *Validation of slip model: flow over cylinder*

A flow past a two dimensional superhydrophobic cylinder has been studied in the present study to verify the applicability of slip boundary conditions. The dimensionless slip length L_s is defined as: $L_s = l_s/D$, Here D is the diameter of the cylinder. As shown in Table 3, we monitored the drag coefficient and the root mean square (RMS) of lift coefficient, which have been compared with the results of [26] at the Reynolds numbers of Re = 100, 180 and dimensionless slip lengths of $L_s = 0.02$, 0.05. The comparison proved an agreement between the current predictions and the existing results with the average relative error of approximately 3% and 5% for the drag coefficient and the RMS of lift coefficient, respectively.

Figure 3 presents the pressure coefficients C_p on the cylindrical surface for dimensionless slip lengths of 0.02 and 0.05, and compares it with the published literatures. Where β represents the angle between the front stagnation point of the cylinder and a point on the cylindrical surface. It can be seen that the pressure coefficients on the cylindrical surface predicted in this paper are in good agreement with the results of Huang *et al.* for both dimensionless slip length conditions. Although there are still some minor differences, the slip model developed in this paper can be considered feasible considering the errors inherent in the numerical calculations.

4. Results and discussions

4.1. *Influence of slip length on the flow characteristics and wake dynamics*

Figure 4(a) shows the drag coefficient as a function of L_s for various Reynolds numbers of 400, 1200, and 2000. Note that the all slip distribution has been adopted in the all case of superhydrophobic spheres in Section 4.1 (as shown in Figure 9(c)), and $L_s = 0$ corresponds to no slip. Results show that the drag coefficient have been reduced from 0.6 to 0.435 by increasing the Reynolds number from 400 to 2000 at $L_s = 0$, which is in good agreement with the published experimental results [40, 41]. In addition, we found that in all cases, the increase of slip length reduces the magnitude of the drag coefficients on the sphere surface. The drag coefficient has

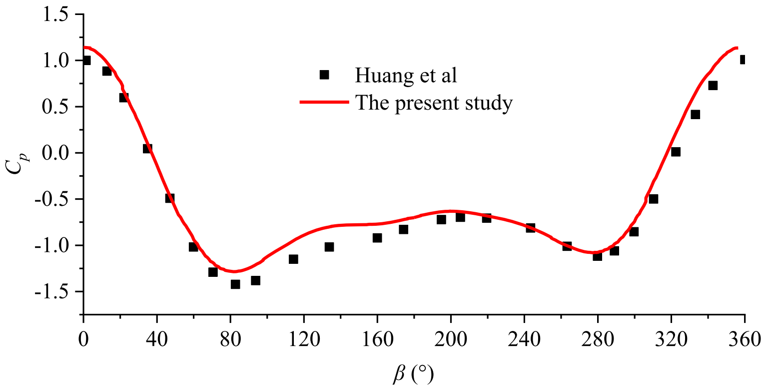

(a) L_s=0.02

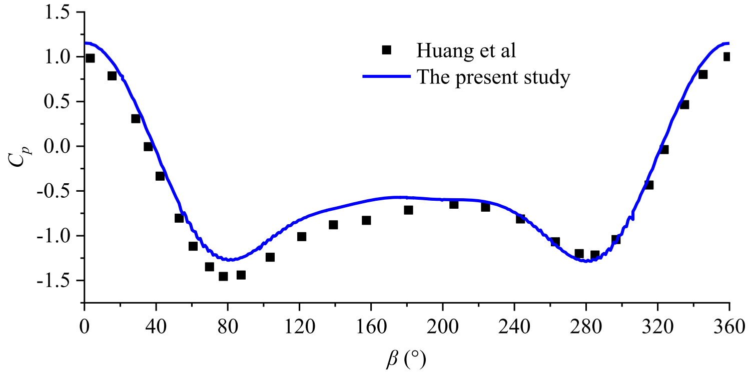

(b) L_s=0.05

Figure 3. Pressure coefficient of cylinder surface under different slip lengths and its comparison with published literature.

been reduced from 0.600, 0.447, 0.430 to 0.140, 0.052, 0.032 for Reynolds number 400, 1200, 2000, by increasing the dimensionless slip length from 0 to 0.2.

Figure 4(b) shows the drag reduction rates at various dimensionless slip lengths for three Reynolds numbers, visualizing the drag reduction effect of the superhydrophobic surface. The drag reduction rate is defined as: $\eta = C_{d0} - C_{ds}/C_{d0}$, where C_{d0} represents the drag coefficient of the no-slip sphere, and C_{ds} is the drag coefficient of the sphere with slip boundary. Results show that the drag reduction rate is proportional to Reynolds numbers and dimensionless slip length. At the maximum dimensionless slip length $L_s = 0.02$, the drag reduction amplitude of Re = 400, 1200 and 200 is up to 76.6%, 88.3% and 92.5% respectively.

Figure 5 illustrates the distribution of the mean shear stress and the pressure coefficient versus the dimensionless slip lengths at Reynolds number of Re = 400. The X–Y cross section through the center of the all slip sphere was selected, and the X-axis is dimensionless by the diameter of the sphere. Comparison of the data obtained from the smooth and all superhydrophobic cases depictes that the amplitude of wall shear stress is continuously reduced with the increase of L_s. As shown in Figure 5(a), the maximume value of the wall shear stress reduces from 14.56 at the dimensionless slip length of 0 to 1.93 at the dimensionless slip length equal to 0.2. This is

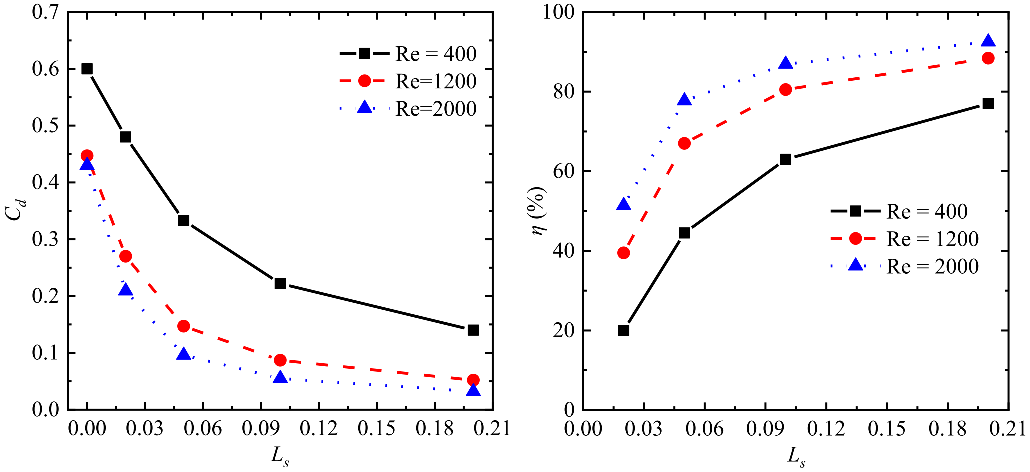

(a) The drag coefficients

(b) The drag reduction rates

Figure 4. The drag coefficient distribution (a) and the drag reduction rates (b) at Reynolds numbers of Re = 400, 1200, 2000 and dimensionless slip lengths of 0, 0.02, 0.05, 0.1 and 0.2.

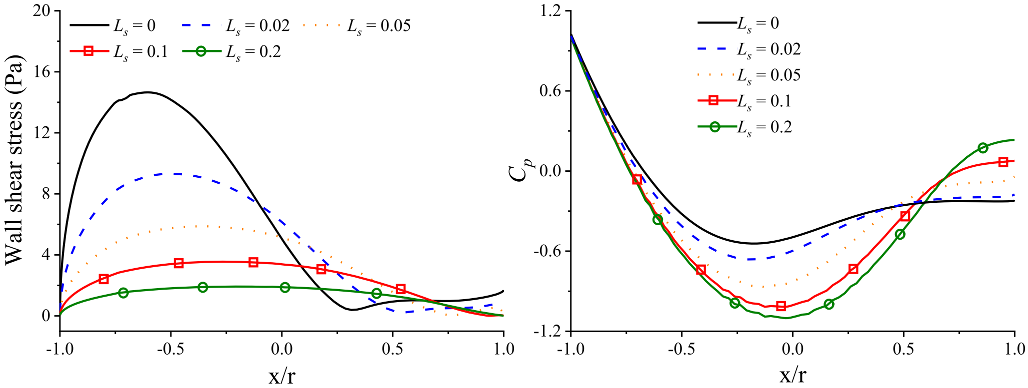

（a）Wall shear stress

（b）The pressure coefficients

Figure 5. Variation of the mean shear stress (a) and the pressure coefficient (b) versus the dimensionless distance between the border and the center of sphere at various dimensionless slip lengths in the range of 0 to 0.2.

because the slope of the velocity profile or the velocity gradient on the wall is reduced by slip velocity, which is proportional to the slip length and generated by the low free energy of the superhydrophobic surface. In addition, it should be noted that the incresing slip length behind the sphere has a minor effect on the distribution of the shear stress along the entire body, which may mean that the superhydrophobic surface behind the sphere can not reduce the drag of the whole body.

In the study of flow around a sphere, the separation of fluid is responsible for the flow pattern and vortex motion in the wake flow field. Therefore, the influence of slip length on the location of the separation point is worth studying, and the separation point at which the shear stress becomes zero. From Figure 5a, the separation point of the smooth sphere is at x/r = 0.31, corresponding to a separation angle of 71.9°, where the separation angle is the angle between the rear stagnation point of the sphere and the separation point. The separation points of hydrophobic spheres with dimensionless slip lengths of 0.02, 0.05 and 0.1 are located at $x/r = 0.54$, $x/r = 0.77$ and $x/r = 0.87$, respectively, corresponding to separation angles of 57.6°, 39.7° and 29.5°, respectively. When the dimensionless slip length continues to increase to 0.2, the separated flow behind the sphere almost disappears. This indicates that an increase in the slip length causes the separation point to move toward the tail of the sphere and decreases the separation angle. This trend is the same as the experimental results of Gruncell [42] and the numerical results of Hongjie Huang *et al.* [26].

The recession of wake region and separation locale is closely related to the pressure distribution on the sphere wall. Figure 5(b) shows the pressure coefficient as a function of L_s at Reynolds number of 400. The fore-aft pressure difference is the main contributor of drag on the body. Here, $L_s = 0$ corresponds to no slip, and has the lowest pressure at $x/r = 1$. For $L_s = 0.2$ the wake pressure is the highest, leading to the most drag reduction. This result is similar to that of the cylinder [26].

In order to better understand the effect of the slip length on flow characteristics, the streamline distributions near the sphere on the X–Y section are shown in Figure 6(a), and the instantaneous variations of drag coefficient in six typical periods are shown in Figure 6(b). Here T is the dimensionless period, defined as $T = t/T_s$, where t is the time after the steady flow field is established, and T_s is the shedding period of the vortex. When the dimensionless slip length $L_s = 0$ (no slip), as shown in Figure 6(a), the back-flow and asymmetric streamline vortices appear behind the sphere, and the length of the recirculation region is about 1.90D. In addition, the drag coefficient in Figure 6(b) fluctuates periodically near the mean value of 0.6, which indicates that alternating periodic vortices shedding occur in the wake. As L_s increases to 0.02, the symmetry of the streamline vortexes is enhanced. At the same time, the length and height of the recirculation region are reduced due to the separation point is shifted towards to the wake. The fluctuation amplitude of the drag coefficient is obviously weakened and the average value of the drag coefficient is reduced to 0.48. However, the vortex shedding period is basically the same as the vortex shedding period of $L_s = 0$, which indicates that the increase of slip length hardly changes the period of wake field at Re = 400 when L_s is small. Completely symmetrical streamline vortexes are formed in the wake when the dimensionless slip length reaches to 0.05. The separation point is further shifted to the direction of the wake, and the recirculation region is further narrowed to 0.93D, which is similar to the result of $L_s = 0.02$. The difference is that the fluctuation of drag coefficient disappeared and is a fixed constant, which implies that the periodic vortex shedding phenomenon no longer appears behind the sphere, and the wake is transformed into a laminar flow. Finally, when the dimensionless slip length is 0.1, the symmetrical streamline vortexes and the recirculation region behind the sphere almost disappear, and the drag coefficient is further decreased to 0.222.

In order to better understand the mechanism of the shrinkage of recirculation region and the disappearance of the drag coefficient fluctuation, it shall be understood that the wake of a smooth sphere presents a turbulent state, and the turbulence is transformed into laminar flow by the increasing slip length, which leads to the continuous decrease of the fluctuation energy. Decreases of the fluctuation energy in the flow field is then responsible for the disappearance of vortex shedding and the contraction of the recirculation region.

The Strouhal number of flow past the sphere is an indicator of the dominant vortex shedding frequencies in the wake of the sphere, and spectral analysis directly reflects the strength of vortices in the wake. Figure 7 displays the variation of the power spectral density versus the Strouhal number of flow past the sphere with the smooth and the superhydrophobic conditions at the Reynolds number of 400. The spectrum is obtained by taking the fast Fourier transformation of the fluctuating drag coefficient. As shown in Figure 7(a), a peak appears at St = 0.139 of the power

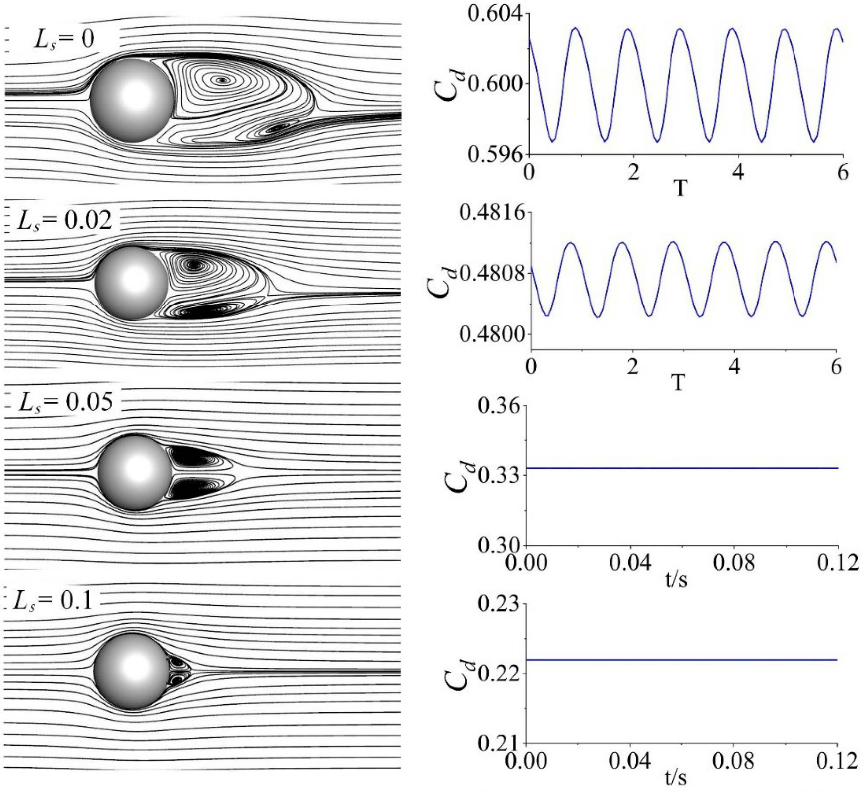

(a) The streamline distributions (b) Time history of the drag coefficient

Figure 6. Flow characteristics at a typical moment when the dimensionless slip length range is 0–0.1: (a) the streamline distributions around the smooth and the superhydrophobic spheres, with emphasis on the evolution of streamline vortex, (b) time history of the drag coefficient on the sphere surface.

spectral distribution, which is caused by the progressive wave motion of the wake with alternate fluctuations [43], indicating that alternating periodic vortex shedding is occurring in the wake. When the dimensionless slip length increases to 0.02, the position of the peak value moves back to St = 0.141, which indicates that the smaller slip length is not enough to have a significant impact on the shedding period of the vortex at Reynolds number of Re = 400. However, it is worth noting that the value of the spectral density is weakened by about two orders of magnitude, and the peak becomes smoother, which result in the decrease of the vortex intensity in the wake. For $L_s \geq 0.05$ (Figure 7(c)), no clear peak is observed by the spectrum analysis, and the value of the power spectral density equals to 0 because the fluctuation energy becomes extremely small. At this time, the periodic vortex shedding phenomenon disappear, and the vortex structure may also be changed. In present paper, only the spectrum analysis with $L_s = 0.05$ is presented, because the spectrum distributions with L_s greater than 0.05 no longer changes.

Figure 8 shows the Q-criterion contours correspond to $Q = 100$ at a typical time when Reynolds number of Re = 400 to visualize the effect of the slip lengths on vortex structure in the sphere wake. When the dimensionless slip length $L_s = 0$, hairpin shaped vortices appear in the wake. As shown in Figures 6 and 7(a) show that the hairpin vortices shedding periodically with a period of 0.018, which is similar to that observed in visualization experiments of Sakamoto [43].

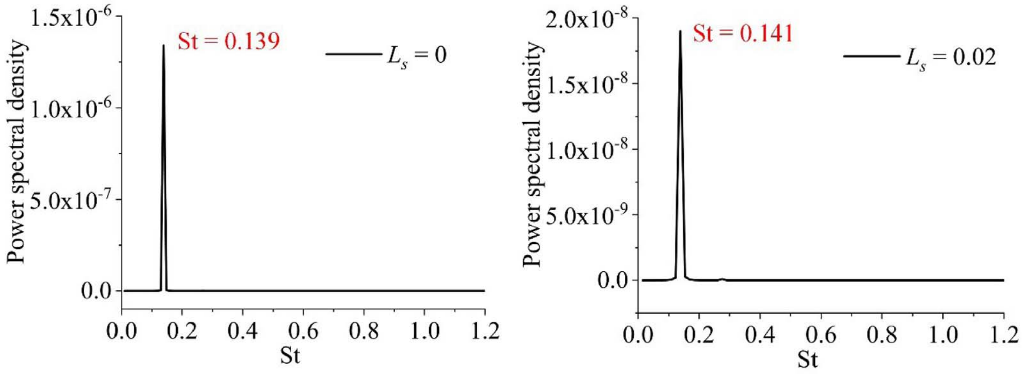

(a) $L_s = 0$ (b) $L_s = 0.02$

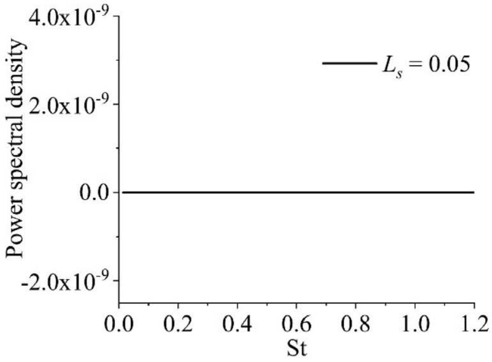

(c) $L_s = 0.05$

Figure 7. Comparison the variation of power spectral density between the no-slip sphere and the superhydrophobic spheres with two slip lengths vlersus the Strouhal number: (a) $L_s = 0$, (b) $L_s = 0.02$, (c) $L_s = 0.05$.

Comparison of the vortex structure of the no-slip and the superhydrophobic spheres concludes that the vortex structure remains unchanged, the vortex shape is not altered when the dimensionless slip length increases to 0.02, but the width and the length of the vortex behind the sphere become narrower and more shortened, respectively (as shown in Figure 8(b)). In addition, the vortex regime changes from hairpin shaped vortex to vortex-ring at a dimensionless slip length L_s of 0.05, as shown in Figure 8(c), the vortex ring appears only in a small region behind the sphere, and with the further increases of the dimensionless slip length, the vortex ring is only compressed in dimension (Figure 8(d)). It is worth noting that the vortex shedding phenomenon is no longer observed, and the stable vortices are formed in the wake of the sphere.

Comparison of these figures suggests that the hairpin-shaped vortices are periodically shed in what is called a regular mode with regularity in strength and frequency, when the imposed dimensionless slip length on walls of sphere is $L_s \leq 0.02$. This is perhaps because the energy entraining into the vortex formation region is very regularly supplied, stored and emitted, as is clearly shown by the fluctuating system of the drag coefficient (Figure 6). This also explains why the vortices shed in succession are of the same strength and frequency. When the imposed dimensionless slip length on walls of sphere is $L_s \geq 0.05$, the vortex ring behind the sphere does not shed or sheds with a very long period, which may be because the energy entering the wake region is too weak to support the vortex ring shedding due to the retreat of the separation point.

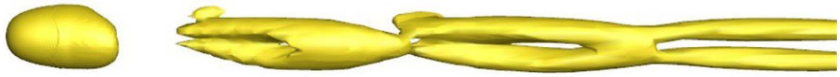

(a) $L_s = 0$

(b) $L_s = 0.02$

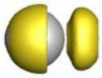

(c) $L_s = 0.05$

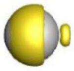

(d) $L_s = 0.1$

Figure 8. Visualize the vortex structures in the wake of the sphere in the form of Q-criterion iso-surfaces ($Q = 100$ s-2), at the dimensionless slip lengths of $L_s = 0, 0.02, 0.05$, and 0.1.

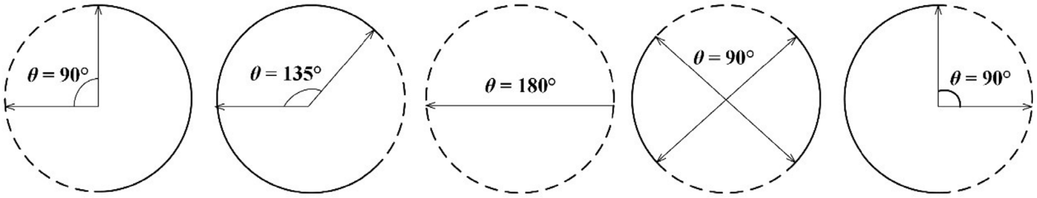

(a) Fore-side slip $\theta = 90°$ (b) Fore-side slip $\theta = 135°$ (c) All slip (d) Flank slip (e) Aft-side slip

Figure 9. Diagram of five types of slip boundary distribution. The solid line region denotes no slip; the dotted line region, slip on the sphere surface. The slip span is denoted by θ, half of the total azimuth which is symmetric about the center axis along the flow direction.

4.2. *The drag reduction mechanism of the various partial-hydrophobic distributions*

The mean shear stress distributions in Figure 5(a) indicates that the application of the superhydrophobicity condition on walls of the sphere has a minor effect on the overall drag reduction, which is worthy of attention in practical engineering, because the reduction of hydrophobic area brings a good prospect of reducing economic cost. Therefore, the influence of the different slip distribution on the drag coefficient and the flow characteristics is investigated in detail in the following sections. As shown in Figure 9, five types of slip distribution are considered: (a) fore-side slip, $\theta = 90°$; (b) fore-side slip, $\theta = 135°$; (c) all slip; (d) flank slip; (e) aft-side slip. The angle of θ is used to describe the superhydrophobic range imposed on the surface of the sphere, and is marked in Figure 9.

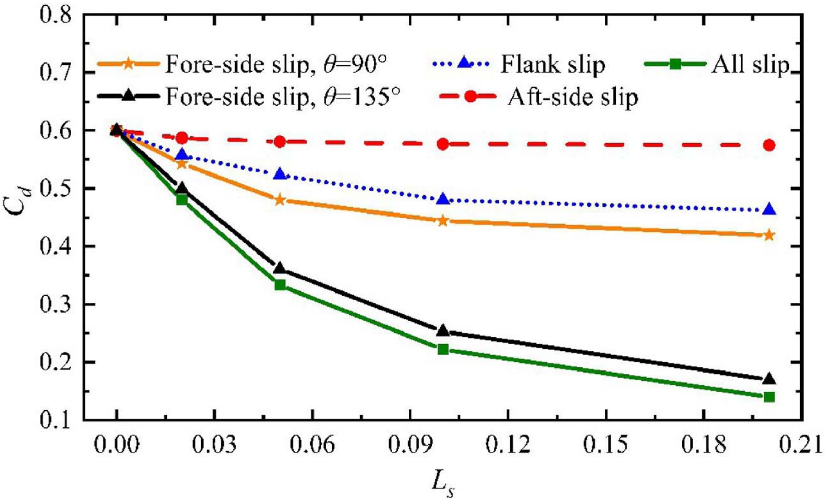

Figure 10. The drag coefficient for the different distributed slip boundary conditions and $L_s = 0, 0.02, 0.05, 0.1, 0.2$. For each case, $L_s = 0$ correspond to no slip and Re = 400. Fore-side slip, $\theta = 135°$ is the most effective on drag reduction in partial-hydrophobic distributions.

In the previous subsection, we have examined in detail the flow with the all slip distribution, and have compared the results with no slip. In what follows, the other four partial-hydrophobic distribution types are studied, and first, the behavior of drag coefficients are examined, which help us establish strategies for slip placement for desired flow control effects. For brevity, we will only present the final results on the drag coefficients at Reynolds number of 400. Next, the drag reduction mechanism of the four partially superhydrophobic distributuions will be discussed. Here Partial-hydrophobic distribution means that only part of the sphere's surface (Figure 9a,b,d,e) is hydrophobic.

As shown in Figure 10, all drag coefficients except the aft-side slip distribution decrease along with an increase in L_s. The drag coefficient distribution obtained by the aft-side slip is close to a horizontal straight line, which further proves that the slip distribution behind the sphere almost has no drag reduction effect. For the flank slip distribution imposes on the wall of the sphere, it is found that the drag reduction is only superior to the aft-side slip, which is completely opposite to the numerical results of the superhydrophobic cylinder. In the study of slip distribution of superhydrophobic cylinder, the flank slip distribution has a better drag reduction than the other slip distributions [27]. The mechanism of the opposite drag reduction effect will be explored later. Furthermore, For the fore-side slip $\theta = 90°$, the drag reduction is still not ideal at various dimensionless slip lengths. Even if L_s is increased to the maximum value of 0.2, the drag reduction rate of 42.8% is still far from 76.7% of the all slip distribution. However, when the angle of θ is increased to 135°, the drag coefficients decrease rapidly at different slip lengths, and the drag reduction effect is the closest to the all slip distribution.

In order to better understand the drag reduction mechanism of the four partially superhydrophobic distributuions, Figure 11 presents the mean shear stress contours on the wall of the sphere at X–Y plane and X–Z plane for diffenrent slip distribution types, Figures 12–14 illustrate the variation of the mean shear stress and the pressure distribution along the dimensionless diameter of the sphere at different slip distributions. Here, the X–Y section through the center of the sphere is adopted. Comparison of these figures shows that by imposing the partially superhydrophobicity condition on walls of the sphere, the interface between slip and no slip inevitably

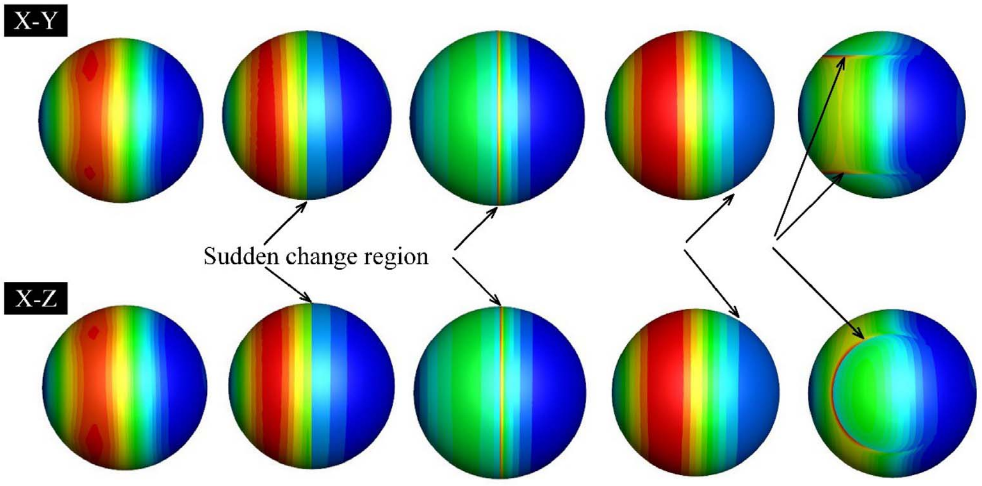

(a) No slip (b) Aft-side slip (c) Fore-side slip $\theta = 90°$ (d) Fore-side slip $\theta = 135°$ (e) Flank slip

Figure 11. The mean shear stress contours at X–Y plane and X–Z plane: (a) no slip; (b) aft-side slip; (c) fore-side slip, $\theta = 90°$; (d) fore-side slip, $\theta = 135°$; (e) flank slip. No slip is a comparative case, and the dimensionless slip length is $L_s = 0.02$.

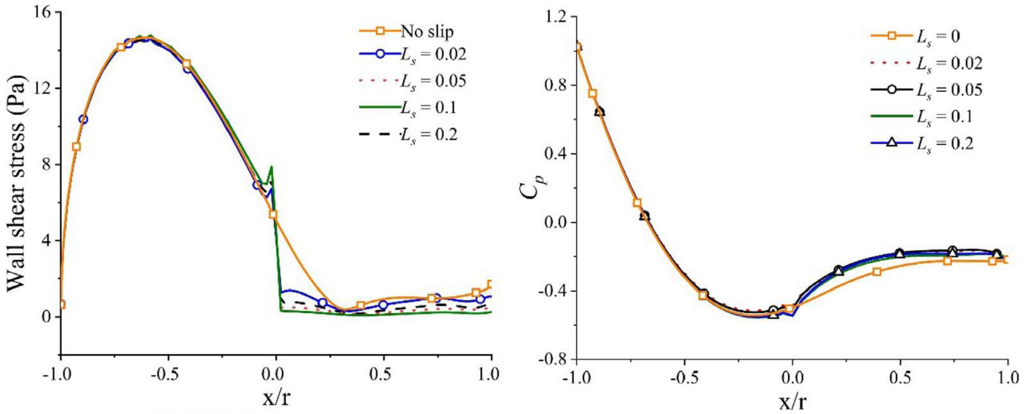

(a) Wall shear stress (b) The pressure coefficients

Figure 12. Variation of the mean shear stress (a) and the pressure coefficient (b) versus the dimensionless diameter of the X–Y section at the dimensionless slip lengths of $L_s = 0, 0.02, 0.05, 0.1, 0.2$ for the aft-side slip distribution.

appears on the wall of the sphere, resulting in a sudden change region appearing on the surface of the partial-hydrophobic sphere and a peak accuring in all the wall characteristic curves. This results are not surprising, as the fluid velocity near the wall experiences a sudden change near this transitional region.

As shown in Figure 12, for the aft-side slip distribution, the peak value appears at $x/r = 0$ (corresponding to $\theta = 90°$ in Figure 9e), i.e., at the interface between slip and no slip, and the amplitude of the peak is almost the same in the dimensionless slip length range of 0–0.2.

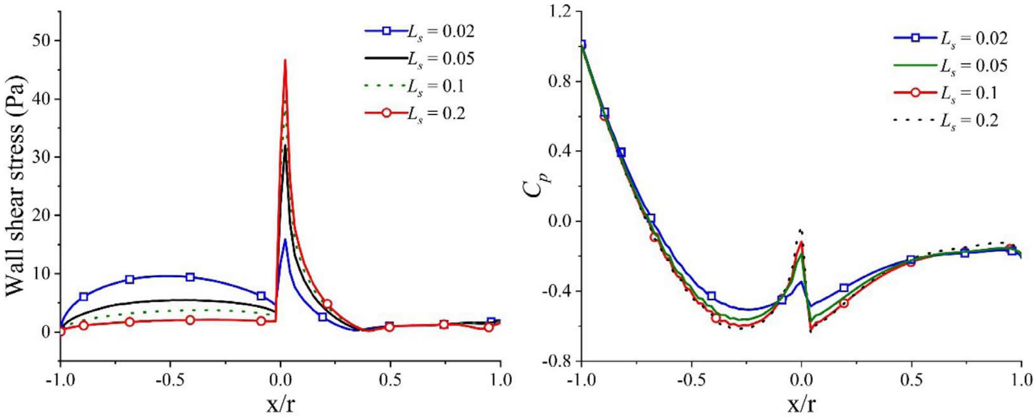

(a) Wall shear stress (b) The pressure coefficients

Figure 13. Variation of the mean shear stress (a) and the pressure coefficient (b) versus the dimensionless diameter of the X–Y section at the different dimensionless slip lengths for the fore-side slip, $\theta = 90°$.

We carefully analyzed the mean shear stress and the pressure coefficient over the surface of the aft-side slip sphere, and found that the numerical results of all aft-side slip cases are similar to that of the no slip sphere except for the sudden change at at $x/r = 0$. Furthermore, at $x/r = 1$, the difference in pressure coefficients at various slip lengths are negligible, which is responsible for the lack of drag reduction of the aft-side slip distribution. Therefore, we suggest that the aft-side slip distribution should be avoided in the drag reduction application of spherical objects.

For the fore-side slip, $\theta = 90°$, although the interface appears at the same position as the aft-side slip distribution, the distribution of wall parameters are completely different, because the slip boundary is placed in the attachment area of the flow, which is more conducive to the reduction of the wall shear stress. As shown in Figure 13, significant peaks occur at the interface, and the amplitude of the peak increases rapidly with the increase of the dimensionless slip length. When L_s increases to 0.2, the peak value of the wall shear stress is up to 46.69 Pa. Furthermore, if inspected closely, the separation point position (the mean shear stress equals to 0) of the flow has hardly changed no matter what the slip length is (Figure 13a). The analysis in Section 4.1 has shown that the wave energy in the flow field decreases with the increase of slip length, and the attenuated wave energy leads to the flow separation point be shifted to the wake direction and the vortex structure to be transformed from hairpin shaped to vortex ring. Therefore, we think that the sudden change at the interface increases the fluctuation energy in the flow field. For all cases of the fore-side slip, $\theta = 90°$, the fluctuation energy generated by the sudden change can offset the reduced fluctuation energy of the slip boundary, thus restraining the backward shift of separation point.

As shown in Figure 14, hairpin shaped vortices always appear in the wake of the sphere at the dimensionless slip length range of 0–0.2. This is beacause the increase of slip length has a minor effect on the fluctuation energy in the flow field, which leads to sufficient energy supply for the generation and shedding of hairpin shaped vortices. In addition, the sudden change narrows the difference of fore-aft pressure difference of the sphere between the different dimensionless slip lengths, as shown in Figure 13(b).

When the angle of the fore-side slip distribution increases to 135°, as shown in Figure 15. The peak becomes less conspicuous at all dimensionless slip lengths. As the dimensionless slip length increases from 0.02 to 0.2, the flow separation point moves back, and the pressure difference

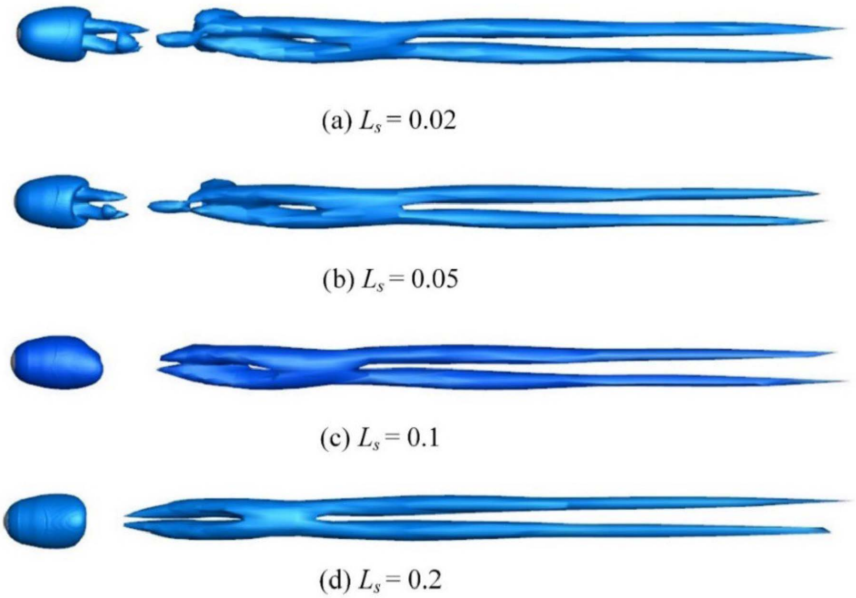

Figure 14. Visualize the vortex structures for the fore-side slip, $\theta = 90°$, in the form of Q-criterion iso-surfaces ($Q = 100$ s-2), at the dimensionless slip lengths of $L_s = 0.02$, 0.05, 0.1 and 0.2.

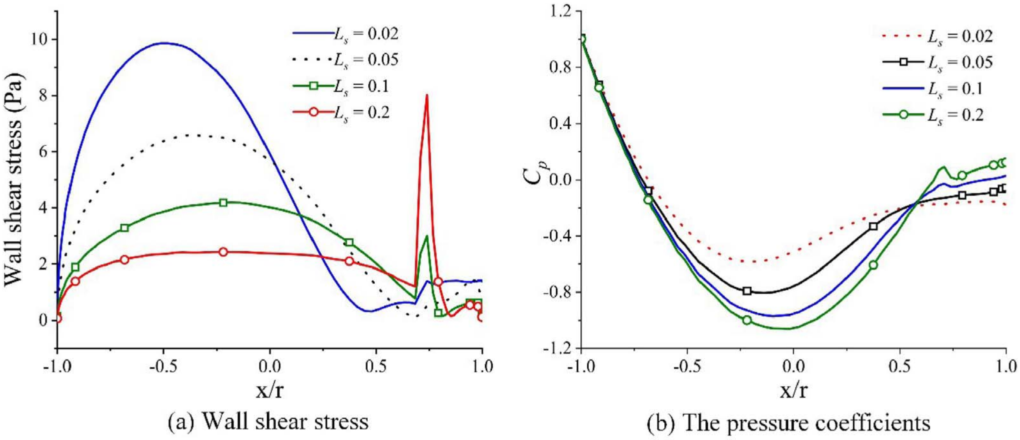

Figure 15. Variation of the mean shear stress (a) and the pressure coefficient (b) versus the dimensionless diameter of the X–Y section at the different dimensionless slip lengths for the fore-side slip, $\theta = 135°$.

between the front and back of the sphere decreased, which are similar to the phenomenon of the all slip distribution. A careful comparison of Figures 13 and 15 shows that, as the angle of θ increased from 90° to 135°, the interface between slip and non-slip be shifted from before to behind the separation point (except $L_s = 0.1$ and $L_s = 0.2$), which may be the main reason for the difference in drag reduction effect. This result indicates that the interface between the slip and no slip is placed in the recirculation region promotes the drag reduction.

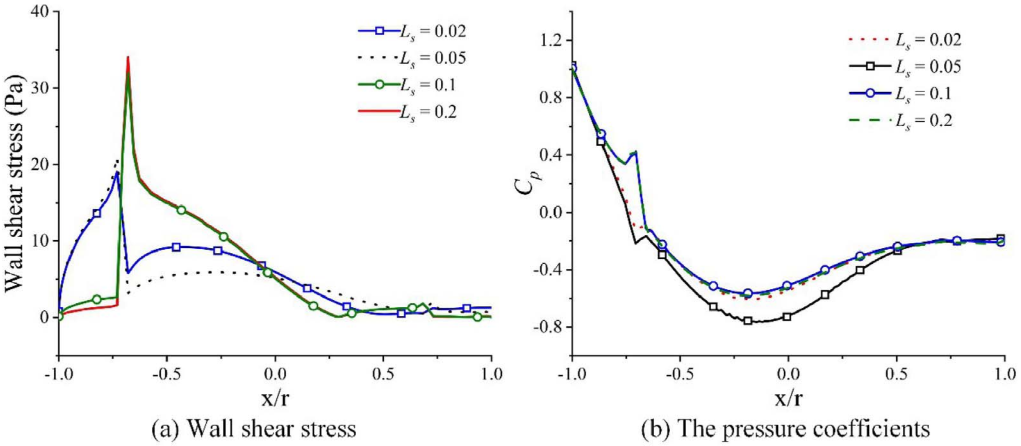

Figure 16. Variation of the mean shear stress (a) and the pressure coefficient (b) versus the dimensionless diameter of the X–Y section at the different dimensionless slip lengths for the flank slip distribution.

With the above findings, the reason for the poor drag reduction of the flank slip distribution is well understood. As shown in Figures 11 and 16, the interfaces of the other three partial-hydrophobic distributions are perpendicular to the incoming flow direction (Figure 11a,b,e). However, the interface of the flank slip distribution is parallel to the flow direction (Figure 11f), which increases the interface number of slip and no slip, widens the sudden change region, greatly strengthens the fluctuation energy in the flow field, and weakens the influence of the slip length on the pressure differential drag (Figure 16b). As shown in Figure 16(a), the separation points with $L_s = 0.1$ and 0.2 are located upstream of the separation points with $L_s = 0.02$ and 0.05, which indicates that at the flank slip distribution, the fluctuation energy generated by sudden change is greater than the fluctuation energy reduced by slip boundary when $L_s \geq 0.1$. Therefore, when applying a superhydrophobic surface to the wall of a spherical object, we recommend reducing the number of interfaces as much as possible, then finding the separation point and covering the entire adhesion region with the superhydrophobic boundary.

5. Conclusions

In this work, we investigated the effects of slip length and slip distribution on flow characteristics past a three-dimensional sphere, and explored the drag reduction mechanism of different slip distributions. After validating the computational simulation results, the slip boundary condition is implemented using User-Defined Functions. The results show that for the all slip distribution, the drag coefficient decreases with the increases of the slip length at Reynolds numbers of Re = 400, 1200, 2000, and the maximum drag reduction rate is up to 92.5%. After that, the flow characteristics of the different slip lengths and slip distributions at Re = 400 are discussed in detail. The conclusions are as follows:

(1) For the all slip distribution, the increases of the slip length can reduce the wall shear stress and the pressure differential drag of the sphere, shifts the separation point of the flow to the downstream, and weakens the fluctuation energy in the flow field continuously. In addition, the increases of the slip length has a minor effect on the wall shear stress behind the sphere.

(2) For the all slip distribution, when the dimensionless slip length increases from 0.02 to 0.05, the asymmetric streamline vortex in the wake is replaced by the symmetrical streamline vortex. The periodically shedding hairpin shaped Vortex is transformed to the vortex ring without shedding.
(3) Among the four types of the partial-hydrophobic distributions, the drag reduction of the fore-side slip, $\theta = 135°$ is the best. In addition, the sudden change of the relevant parameters occurs at the interface between slip and no slip, which increases the fluctuation energy in the flow field, and the fluctuation energy generated by the sudden change is positively related to the number of the interface and the value of the slip length.
(4) For the partial slip distribution, the separation point is closely related to the wave energy. When the fluctuation energy generated by sudden change is less than, equal to or greater than the fluctuation energy reduced by slip boundary, the separation point moves downstream, stationary and upstream respectively.

Conflicts of interest

Authors have no conflict of interest to declare.

Acknowledgements

This research did not receive any specific grant from funding agencies in the public, commercial, or not-for-profit sectors.

References

[1] C. X. Jiang, S. L. Li, F. C. Li, W. Y. Li, “Numerical study on axisymmetric ventilated supercavitation influenced by drag-reduction additives”, *Int. J. Heat Mass Transfer* **115** (2017), p. 62-76.

[2] C.-X. Jiang, Z.-J. Shuai, X.-Y. Zhang, W.-Y. Li, F.-C. Li, “Numerical study on evolution of axisymmetric natural supercavitation influenced by turbulent drag-reducing additives”, *Appl. Therm. Eng.* **107** (2016), p. 797-803.

[3] A. Rastegari, R. Akhavan, “On the mechanism of turbulent drag reduction with super-hydrophobic surfaces”, *J. Fluid Mech.* **773** (2015), article no. R4.

[4] M. Dhiman, R. Gupta, K. A. Reddy, “Hydrodynamic interactions between two side-by-side Janus spheres”, *Eur. J. Mech. (B/Fluids)* **87** (2021), p. 61-74.

[5] W.-M. Zhang, G. Meng, X. Wei, “A review on slip models for gas microflows”, *Microfluid. Nanofluid.* **13** (2012), p. 845-882.

[6] L. A. Ju, A. Jy, H. A. Zheng, Y. B. Hang, A. Ky, A. Yg, “Numerical investigation on the formation mechanism of ventilated cavitation with gas jet cavitator”, *Eur. J. Mech. (B/Fluids)* **87** (2021), p. 37-46.

[7] W. U. Hao, O. Yongpeng, Y. E. Qing, “Experimental study of air layer drag reduction on a flat plate and bottom hull of a ship with cavity”, *Ocean Eng.* **183** (2019), p. 236-248.

[8] J. Lee, H. Kim, H. Park, “Effects of superhydrophobic surfaces on the flow around an NACA0012 hydrofoil at low Reynolds numbers”, *Exp. Fluids* **59** (2018), p. 1-18.

[9] Y. L. Xiong, D. Yang, “Influence of slip on the three-dimensional instability of flow past an elongated superhydrophobic bluff body”, *J. Fluid Mech.* **814** (2017), p. 69-94.

[10] T. Jung, H. Choi, J. Kim, “Effects of the air layer of an idealized superhydrophobic surface on the slip length and skin-friction drag”, *J. Fluid Mech.* **790** (2016), article no. R1.

[11] B. Zeinali, J. Ghazanfarian, B. Lessani, “Janus surface concept for three-dimensional turbulent flows”, *Comput. Fluids* **170** (2018), p. 213-221.

[12] W. Barthlott, C. Neinhuis, “Purity of the sacred lotus, or escape from contamination in biological surfaces”, *Planta* **202** (1997), p. 1-8.

[13] D. Song, R. J. Daniello, J. P. Rothstein, “Drag reduction using superhydrophobic sanded Teflon surfaces”, *Exp. Fluids* **55** (2014), article no. 1783.

[14] J. Zhang, H. Tian, Z. Yao, P. Hao, N. Jiang, “Evolutions of hairpin vortexes over a superhydrophobic surface in turbulent boundary layer flow”, *Phys. Fluids* **28** (2016), article no. 095106.

[15] R. J. Daniello, N. E. Waterhouse, J. P. Rothstein, “Drag reduction in turbulent flows over superhydrophobic surfaces”, *Phys. Fluids* **21** (2009), article no. 085103.

[16] J. Ou, B. Perot, J. P. Rothstein, “Laminar drag reduction in microchannels using ultrahydrophobic surfaces”, *Phys. Fluids* **16** (2004), p. 4635-4643.

[17] J. Ou, J. P. Rothstein, “Direct velocity measurements of the flow past drag-reducing ultrahydrophobic surfaces”, *Phys. Fluids* **17** (2005), article no. 103606.

[18] M. B. Martell, J. B. Perot, J. P. Rothstein, “Direct numerical simulations of turbulent flows over superhydrophobic surfaces”, *J. Fluid Mech.* **620** (2009), p. 31-41.

[19] J. Zhang, H. Tian, Z. Yao, P. Hao, N. Jiang, “Mechanisms of drag reduction of superhydrophobic surfaces in a turbulent boundary layer flow”, *Exp. Fluids* **56** (2015), article no. 179.

[20] W. Abu Rowin, S. Ghaemi, “Streamwise and spanwise slip over a superhydrophobic surface”, *J. Fluid Mech.* **870** (2019), p. 1127-1157.

[21] M. Castagna, N. Mazellier, A. Kourta, “On the onset of instability in the wake of super-hydrophobic spheres”, *Int. J. Heat Fluid Flow* **87** (2021), article no. 108709.

[22] C. Navier, “Mémoire sur les lois du mouvement des fluides”, *Mem. Acad. R. Sci. Inst. Fr.* **6** (1823), p. 389-440.

[23] D. Legendre, E. Lauga, J. Magnaudet, “Influence of slip on the dynamics of two-dimensional wakes”, *J. Fluid Mech.* **633** (2009), p. 437-447.

[24] R. Daniello, P. Muralidhar, N. Carron, M. Greene, J. P. Rothstein, “Influence of slip on vortex-induced motion of a superhydrophobic cylinder”, *J. Fluids Struct.* **42** (2013), p. 358-368.

[25] I. W. Seo, C. G. Song, “Numerical simulation of laminar flow past a circular cylinder with slip conditions”, *Int. J. Numer. Methods Fluids* **68** (2012), p. 1538-1560.

[26] H. Huang, M. Liu, H. Gu, X. Li, X. Wu, F. Sun, “Effect of the slip length on the flow over a hydrophobic circular cylinder”, *Fluid Dyn. Res.* **50** (2018), article no. 025515.

[27] D. Li, S. Li, Y. Xue, Y. Yang, W. Su, Z. Xia, Y. Shi, H. Lin, H. Duan, “The effect of slip distribution on flow past a circular cylinder”, *J. Fluids Struct.* **51** (2014), p. 211-224.

[28] B. Zeinali, J. Ghazanfarian, “Turbulent flow over partially superhydrophobic underwater structures: The case of flow over sphere and step”, *Ocean Eng.* **195** (2020), article no. 106688.

[29] R. Pit, H. Hervet, L. Léger, “Direct experimental evidence of slip in hexadecane: solid interfaces”, *Phys. Rev. Lett.* **85** (2000), no. 5, p. 980-983.

[30] L. I. Jian, M. Zhou, L. Cai, Y. Xia, U. Yuan, “Run center for photon manufacturing science and technology, on the measurement of slip length for liquid flow over super-hydrophobic surface”, *China Sci. Bull.* **54** (2009), no. 24, p. 4560-4565.

[31] C. Lee, C. Kim, “Influence of surface hierarchy of superhydrophobic surfaces on liquid slip”, *Langmuir* **27** (2011), p. 4243-4248.

[32] Y. Murai, “Frictional drag reduction by bubble injection”, *Exp. Fluids* **55** (2014), article no. 1773.

[33] R. Deng, C. H. Wang, K. A. Smith, “Bubble Behavior in a Taylor Vortex”, *Phys. Rev. E* **73** (2006), article no. 036306.

[34] P. Sooraj, M. S. Ramagya, M. H. Khan, A. Sharma, A. Agrawal, “Effect of superhydrophobicity on the flow past a circular cylinder in various flow regimes”, *J. Fluid Mech.* **897** (2020), article no. A21.

[35] Q. Ren, Y. L. Xiong, D. Yang, J. Duan, “Flow past a rotating circular cylinder with superhydrophobic surfaces”, *Acta Mech.* **229** (2018), p. 3613-3627.

[36] J. Liu, J. Yu, Z. Yang, Z. He, Y. Li, “Numerical investigation of shedding dynamics of cloud cavitation around 3D hydrofoil using different turbulence models”, *Eur. J. Mech. (B/Fluids)* **85** (2021), p. 232-244.

[37] J. S. Wu, G. M. Faeth, “Sphere wakes in still surroundings at intermediate Reynolds numbers”, *AIAA J.* **31** (1993), p. 1448-1455.

[38] A. G. Tomboulides, S. A. Orszag, G. E. Karniadakis, “Direct and large-eddy simulations of axisymmetric wakes”, in *AIAA Aerospace Sciences Meeting & Exhibit*, 1993.

[39] R. H. Magarvey, R. L. Bishop, “Transition ranges for three-dimensional wakes”, *Can. J. Phys.* **39** (1961), p. 1418-1422.

[40] H. J. Kim, P. A. Durbin, “Observations of the frequencies in a sphere wake and of drag increase by acoustic excitation”, *Phys. Fluids* **31** (1988), article no. 3260.

[41] F. W. Roos, W. W. Willmarth, “Some experimental results on sphere and disk drag”, *AIAA J.* **9** (1971), p. 285-291.

[42] B. R. K. Gruncell, N. D. Sandham, G. McHale, “Simulations of laminar flow past a superhydrophobic sphere with drag reduction and separation delay”, *Phys. Fluids* **25** (2013), article no. 043601.

[43] H. Sakamoto, H. Haniu, “A study on vortex shedding from spheres in a uniform flow”, *J. Fluids Eng.* **112** (1990), p. 386-392.